



# How surface charges affect interdroplet freezing

Siyan Yang<sup>a,b,1</sup>, Bingqiang Ji<sup>c,1</sup> 🗓, Yawei Feng<sup>b,1</sup> 🗓, Yuankai Jin<sup>a</sup> 🗓, Wanghuai Xu<sup>a</sup>, Jingyi Lu<sup>a</sup>, Xuezhi Qin<sup>a</sup>, Huanhuan Zhang<sup>a</sup>, Mingyu Li<sup>b</sup>, Zhenyu Xu<sup>b</sup>, Xiaonan Liu<sup>a</sup>, Luqing Xu<sup>d</sup>, Dehui Wang<sup>d</sup>, Rongfu Wen<sup>e</sup>, Zhenying Wang<sup>f</sup>, Steven Wang<sup>b</sup>, Xuehu Ma<sup>e</sup>, and Zuankai Wang<sup>a2</sup> 📵

Affiliations are included on p. 8.

Edited by Yonggang Huang, Northwestern University-Evanston, Glencoe, IL; received April 3, 2025; accepted May 14, 2025

The freezing of droplets on surfaces is closely relevant with various industrial processes such as aviation, navigation, and transportation. Previous studies mainly focus on physiochemically heterogeneous but electrically homogeneous surfaces, on which the presence of vapor pressure gradient between droplets is the predominant mechanism for interdroplet freezing bridging, propagation, and eventual frosting across the entire surface. An interesting yet unanswered question is whether electrostatic charge on surfaces affects freezing dynamics. Here, we find an interdroplet freezing relay (IFR) phenomenon on electrically heterogeneous surfaces that exhibits a three-dimensional, in-air freezing propagation pathway and an accelerated freezing rate. Theoretical and experimental investigations demonstrate that this phenomenon originates from the presence of surface charge gradient established between the frozen droplet and neighboring water droplet, which leads to a spontaneous shooting of desublimated ice needles from the frozen droplet and then triggers the freezing of neighboring water droplet in in-air manner. We further demonstrate its generality across various dielectric substrates, liquids, and droplet configurations. Our work enriches conventional perspectives on droplet freezing dynamics and emphasizes the pivotal role of electrostatics in designing passive anti-icing and antifrosting materials.

droplet freezing | icing | surface charge

Droplet freezing is ubiquitous in nature and is closely relevant to a vast array of processes, spanning aviation, navigation, transportation, and thermal management (1–3). Over the past decade, extensive progress has been achieved in our fundamental understanding and controlling freezing dynamics on a wide range of surfaces (4–7). Despite the diversity in engineered surfaces and the manifested phenomena as well as the complexity in freezing mechanisms (6–10), droplet freezing on surfaces appears to reveal an interesting common pattern, characterized by manifesting interdroplet freezing within droplet clusters along the surface (11, 12). Conventional understanding holds that the interdroplet freezing bridging process is mainly driven by vapor pressure gradient built between frozen and unfrozen droplets, in which the frozen droplet serves as a sink to draw vapor from nearby unfrozen water droplets and ultimately triggers the freezing of the entire droplets (11–13).

Despite extensive efforts, existing studies mainly focus on physiochemical heterogeneous and electrically homogeneous surfaces (14-16). Unlike physiochemical attributes such as topography and wettability which are static, the electrostatic properties of surfaces, such as polarity and potential, can be dynamically modulated through charging and discharging (17, 18). Despite their extremely small size (10<sup>-15</sup> m) (19), surface charges exhibit extraordinary abilities to influence the behaviors of droplets and bubbles with applications ranging from fluid dynamics to energy harvesting (20-27). Surface charges also generate strong electrostatic forces to overcome adhesion, gravity, or drag forces that are imposed to solid particles, enabling fascinating dynamics such as locomotion (28), aggregation (29), saltation (30), or flight (31).

In this work, we uncover an interdroplet freezing relay (IFR) phenomenon, referred to as IFR, on electrically heterogeneous surfaces. The surface charge gradient established on the electrically heterogeneous surfaces leads to spontaneous and rapid shooting of desublimated ice needles from the frozen droplet, which triggers the freezing of neighboring water droplets. Unlike conventional freezing bridging process mainly regulated by physiochemical surface attributes, this phenomenon occurs beyond the surface plane into three-dimensional space, showcasing remarkable robustness and scalability across a range of dielectric substrates and diverse liquids.

#### **Results and Discussion**

**Electrostatics-Driven IFR via Ice Needle Shooting.** Different from the chemically or structurally modified substrates used in previous droplet freezing studies, we chose polytetrafluoroethylene (PTFE) as the substrate in our experiment owing to its high

## **Significance**

Freezing propagation among droplets has been widely understood as a process occurring in two-dimensional space and driven by interdroplet vapor pressure gradient, tuning which mainly relies on refining physio-chemically heterogeneous but electrically homogeneous surfaces. Here, we probe droplet freezing dynamics on electrically heterogeneous surface and find an interdroplet freezing relay (IFR) phenomenon that exhibits a three-dimensional freezing propagation pathway. This new mode of propagation accelerates the freezing process and is robust across different substrates, liquids, and droplet arrangements. Our finding highlights the critical yet unexplored role of electrostatics in droplet icing and offers a strategy for controlling surface freezing at scale.

Author contributions: S.Y., B.J., Y.F., Y.J., and Z.W. designed research; S.Y., Y.F., J.L., M.L., Z.X., X.L., and L.X. performed research; S.Y., B.J., Y.J., H.Z., and R.W. contributed new reagents/analytic tools; S.Y., W.X., X.Q., and D.W. analyzed data; and S.Y., B.J., Y.F., W.X., Z.W., S.W., X.M., and Z.W. wrote the paper.

The authors declare no competing interest.

This article is a PNAS Direct Submission.

Copyright © 2025 the Author(s). Published by PNAS. This article is distributed under Creative Commons Attribution-NonCommercial-NoDerivatives License 4.0

<sup>1</sup>S.Y., B.J., and Y.F. contributed equally to this work.

<sup>2</sup>To whom correspondence may be addressed. Email: zk.wang@polyu.edu.hk.

This article contains supporting information online at https://www.pnas.org/lookup/suppl/doi:10.1073/pnas. 2507849122/-/DCSupplemental.

Published June 18, 2025

triboelectrification ability (20, 32). By depositing a conductive copper thin film on the left region of the PTFE substrate to dissipate inherent electric charges and cutting a 1 mm width groove in the center of the substrate, the originally electrically homogeneous surface became electrically heterogeneous, in which the left region was neutral, whereas the right region was charged. Fig. 1A shows the snapshot of two frozen droplets on the modified substrate, both at identical temperatures but with differing surface charge properties. Specifically, a 10 µl droplet was first placed on the copper-coated cold region to freeze. Ice needles were observed to form on the droplet when an additional water droplet approached it from the above due to desublimation driven by vapor gradient. An intriguing phenomenon was observed when another 10 µl water droplet was deposited on the PTFE region, characterized by the continuous shooting of ice needles from the frozen droplet toward the adjacent water droplet and triggered its freezing (Fig. 1 A and B and Movie S1). Such an IFR phenomenon may be attributed to the presence of a surface charge gradient across the electrically heterogeneous substrate, which is in contrast with conventional freezing bridging phenomenon that is typically driven by vapor pressure gradient.

To confirm the role of surface charge gradient on the occurrence of the IFR phenomenon, we suspended and grounded the droplet that was previously rested on copper-covered region, ensuring a well-defined charge gradient without substrate's cooling-induced droplet freezing (Fig. 1C and SI Appendix, Fig. S1 A and B). Throughout the experiment, both the substrate (SI Appendix, Fig. S1C) and the pendant droplet (SI Appendix, Fig. S1D) were maintained below the freezing point; notably, the pendant droplet remained in a liquid state, as evidenced by the inset in SI Appendix, Fig. S1D. After 360 s of freezing for the sessile droplet, a sudden localized recalescence event was observed on the pendant droplet surface, followed by its gradual solidification (Movie S1). As the recalescence process is accompanied by a large amount of heat release (9, 13, 33), we further employed infrared imaging technique, which captured a rapid temperature rise from -2 to 0 °C on the pendant droplet's surface (SI Appendix, Fig. S2A and Movie S2), corroborating the recalescence trigger. Careful inspections revealed that this partial freezing occurred precisely upon the ice needle shoots from the frozen droplet toward the pendant droplet, also in an out-of-plane manner. In contrast, Fig. 1D shows a different scenario when the PTFE substrate was electrostatically neutralized, where the pendant droplet started to freeze at a much later stage (after 820 s). The freezing of the droplet was only triggered by direct contact with the advancing ice needle, which was reminiscent of the traditional interdroplet freezing bridging (11, 34). Therefore, this stark contrast serves as compelling evidence that surface charges play a pivotal role in triggering ice needle shooting-induced freezing.

High-speed imaging provided further insights into this IFR phenomenon. As shown in Fig. 1E and SI Appendix, Fig. S2B, the velocity of ice needle shooting scaled linearly with droplet spacing  $(v \sim S)$  and was nearly five orders of magnitude greater than the speed of conventional freezing bridging (16, 35)  $(v \sim S^{-1})$ , details in SI Appendix). Although minutes were required for ice needle growth, the overall freezing delay for the pendant droplet was significantly shorter than conventional freezing bridging, and this effect amplifies as droplet spacing increases (Fig. 1F). This finding substantiates that the occurrence of ice needle shooting significantly accelerates the freezing propagation between droplets, outpacing the conventional freezing bridging mode.

# **Generality of Electrostatics-Driven IFR via Ice Needle Shooting.** We further demonstrated the generality of ice needle shooting-induced IFR across a wide range of conditions. Fig. 2*A* illustrates the relationship between the ice needle shooting distance—equivalent

to the droplet spacing (S)—and the electrostatic capacity of the substrate. This phenomenon could spontaneously occur on numerous dielectric materials with diverse charging capabilities negatively charged substrates like PTFE, polystyrene (PS), and polyethylene terephthalate (PET), as well as positively charged ones such as thermoplastic polyurethane (TPU), glass, and nylon (details in SI Appendix, Table S1 and Fig. S3A and Movie S3). Notably, the highest ice needle shooting distance,  $S_{\text{max}}$ , corresponding to the maximum droplet spacing allowing ice needle shooting, correlated positively with the material's surface charge density. PTFE, with the ability to generate the highest negative surface charge density (-190 nC/m<sup>2</sup>, normalized to -1) (36, 37), enabled the largest  $S_{\text{max}}$  of 2.7 mm. In contrast, conductive substrates like copper and aluminum, as well as dielectric substrates that underwent electroneutralization treatments, such as heating to 80 °C or wiping with alcohol, referred to as PTFE-0 and Nylon-0, respectively (see SI Appendix, Table S1 for details), were not able to induce ice needle shooting, with *S*=0 mm.

Beyond pure water, further experiments revealed that ice needle shooting could also trigger the freezing of a diverse range of water sources, including tap water, rainwater, river water, seawater, NaOH solution, and even saturated NaCl solution, when using a PTFE substrate. Polar liquids, including dimethyl sulfoxide, ethyl alcohol, ethylene glycol, isopropanol, acetone, and acetic acid, also supported the ice needle shooting behavior (Fig. 2B). In contrast, nonpolar liquids, unable to be effectively electrostatically induced because of lacking permanent dipole moments, could not induce ice needle shooting, further confirming the critical role of surface charges in triggering the shooting behavior. Additionally, this phenomenon persisted under diverse spatial arrangements, extending beyond horizontally and vertically aligned droplet configurations to droplets of various forms (SI Appendix, Fig. S3 B-E and Movie S3). It is worth mentioning that when the ambient humidity exceeds 40%, condensation tends to occur on the substrate, which leads to the screening of surface charges. As a result, the ice needle shooting phenomenon is suppressed, further confirming the critical role of surface charges. Together, these findings not only confirm the widespread occurrence of ice needle shooting in charge-enriched systems but also offer a perspective for designing anti-icing and antifrosting materials. While traditional approaches have primarily focused on tuning surface structures or chemical properties, our study further highlights the critical role of surface charges, which warrants attention in future designs.

**Mechanism for Launching the Ice Needle Shooting.** We then unraveled the underlying physics driving the ice needle shooting. Due to electrostatic induction, an uneven electrostatic field surrounding the two droplets was naturally formed, which intensifies at the opposing droplet surfaces. This characteristic was validated through COMSOL simulations (*SI Appendix*, Fig. S4 *A–D*). As a result, an intensified electrostatic force was generated to rupture the growing ice needle, triggering its shooting. Once shooting occurs, the in-air trajectory was entirely dominated by the electric field, which was verified through high-speed imaging (*SI Appendix*, Fig. S4 *D* and *E* and Movie S4).

To ensure the controlled charge accumulation and stable electric field, we continued to replace the dielectric PTFE substrate with a conductive copper substrate (–10 °C) connected to a direct-current power supply (Fig. 3A). Such a configuration enabled us to quantitatively analyze the mechanism responsible for ice needle shooting. We found that the ice needle shooting threshold is governed by the interplay between the interdroplet spacing S and applied voltage U, as shown in Fig. 3B. Notably, U and the largest interdroplet spacing for ice needle shooting,  $S_{\max}$ , exhibit

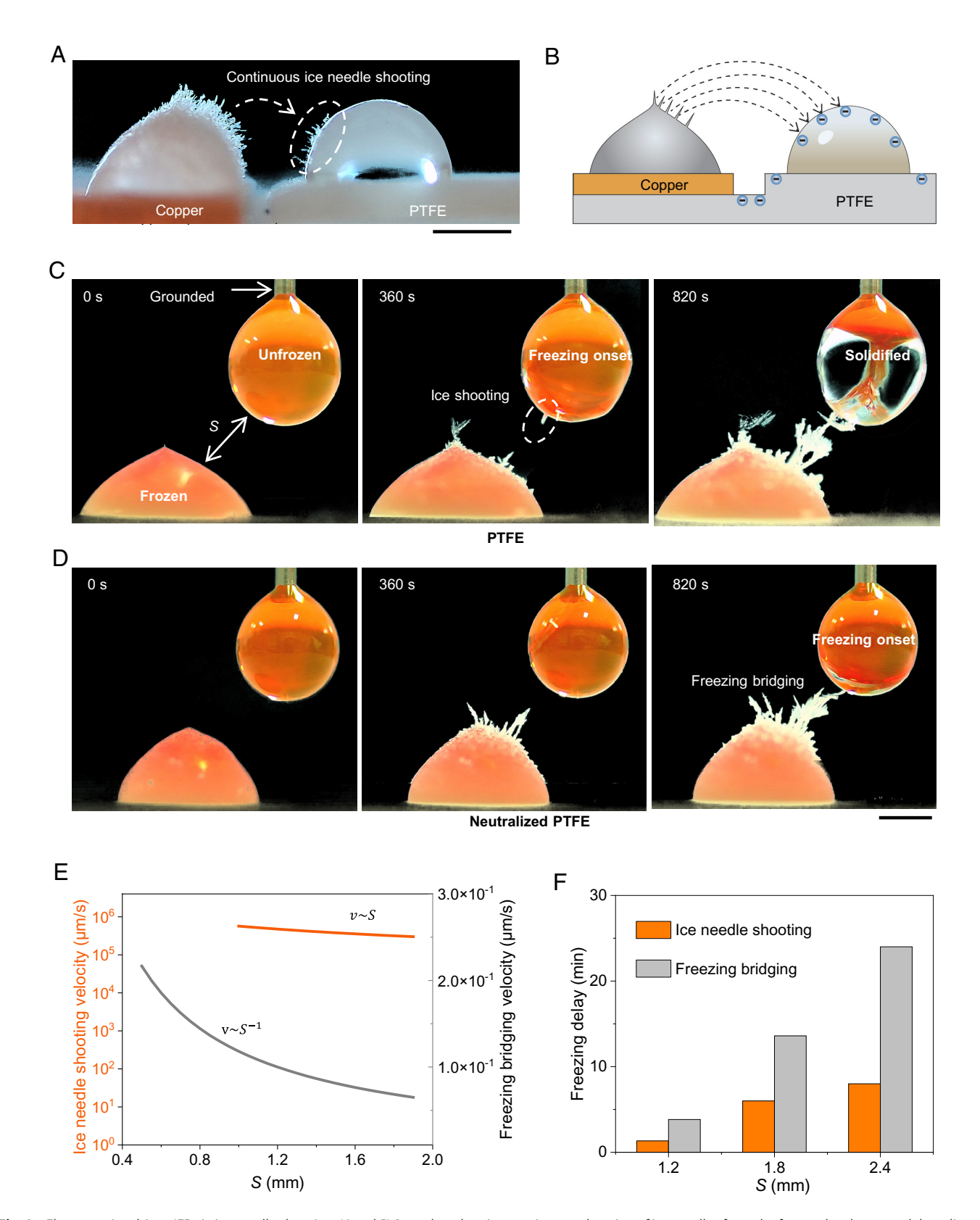
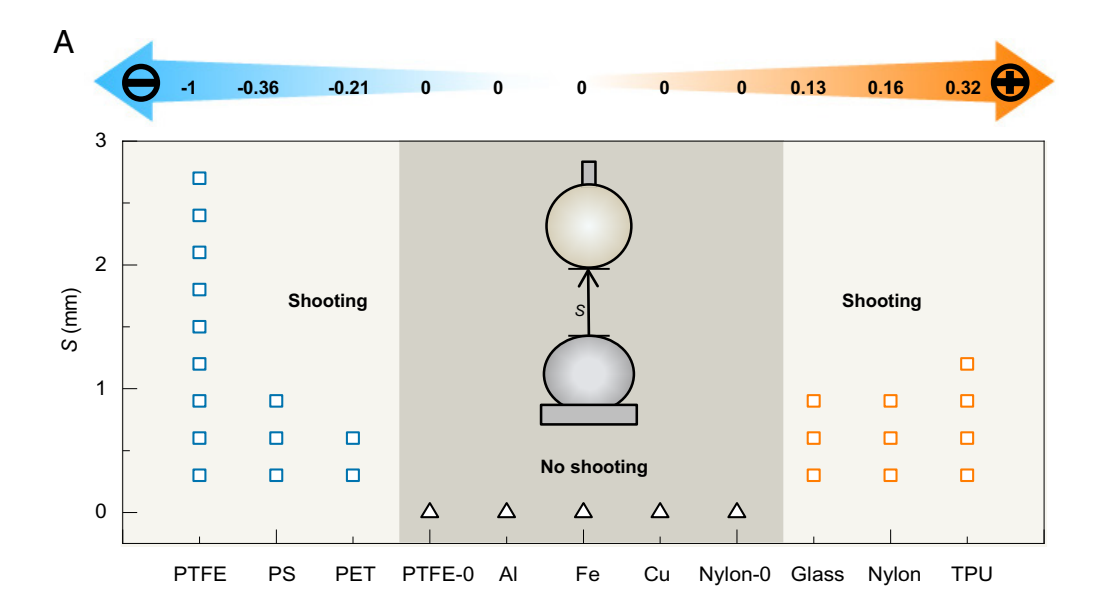


Fig. 1. Electrostatics-driven IFR via ice needle shooting. (A and B) Snapshot showing continuous shooting of ice needles from the frozen droplet toward the adjacent water droplet. The two droplets were deposited on the modified substrate, both under identical temperatures but with differing surface charge properties. (C) After 360 s of freezing for the sessile droplet, the pendant droplet began to freeze precisely upon the ice needle shoots from the frozen sessile droplet on the PTFE substrate toward the pendant droplet. (D) The pendant droplet started to freeze after 820 s, triggered by direct contact with the advancing ice needle grown from the sessile droplet on an electrostatically neutralized PTFE substrate. (E) Comparison of velocity and (P) overall freezing delay between interdroplet ice needle shooting and freezing bridging. The freezing bridging of ice needle shooting was up to five orders of magnitude faster than that of conventional freezing bridging, while the overall freezing delay of the pendant droplet induced by ice needle shooting was significantly compared to freezing bridging. Ambient temperature: 10 to 15 °C; relative humidity: less than 40%; surface temperature: -10 °C; pendant droplet temperature: -2 to -0.5 °C. (Scale bar, 1 cm.)



Polarity	Liquid resources	Shooting
Water resources (polar)	DI water	✓
	Tap water	✓
	Rain water	✓
	River water	✓
	Sea water	✓
	Saturated NaCl	✓
	NaOH (0.01 mol/L)	✓
Other liquids (polar)	Dimethyl sulfoxide	✓
	Ethyl alcohol	✓
	Ethylene glycol	✓
	Isopropanol	✓
	Acetone	✓
	Acetic acid	✓
Other liquids (nonpolar)	Petroleum ether	×

Fig. 2. Generality of electrostatics-driven IFR via ice needle shooting. (A) Phase diagram illustrating the relationship between the ice needle shooting distance—equivalent to the droplet spacing (S)—and the electrostatic capacity of the substrate. PTFE-0 and Nylon-0 refer to dielectric surfaces subjected to electroneutralization treatments. (B) Ice needle shooting facilitated by various polar liquids, while being inhibited in nonpolar ones.

a linear relationship because of the balance of electric force and cohesive force that act on the growing ice needle. As the needle elongates and accumulates surface charges, the upward electrostatic force  $F_e$  increases (SI Appendix, Fig. S5 A and B). On the other hand, the cohesive force  $F_{co}$  that is against the driving force serves to maintain the structural integrity of the ice needle. In our analysis, the gravitational force is negligible (see SI Appendix, Fig. S5 C and SI Appendix). Once  $F_e$  surpasses the maximum cohesive force  $F_c$  (38, 39), the ice needle detached abruptly from the frozen droplet and shot toward the pendant water droplet (Fig. 3*C*).

The electrostatic force  $F_e$  is expressed as (31)  $F_e = E\sigma A = S^2 \varepsilon k A$ , where E denotes the electric field intensity,  $\varepsilon_0$  is the permittivity of vacuum  $(8.854 \times 10^{-2} \text{ F/m})$ , k is a dielectric constant calculated to be 3.37 in this system (SI Appendix, Fig. S6 A-D and *SI Appendix*), and *A* is the surface area of the ice needle. Due to the spatially uneven distribution of E in the system, the precise

shooting location of the ice needles was identified to determine the exact value of E. As over 95% of shooting events occurred at the apex of the frozen droplet, with an azimuth angle of  $\alpha = 90 \pm$ 10°, regardless of the applied voltage (Fig. 3D) and droplet size (Fig. 3E), justifying the assumption of an identical E for all ice needles on the droplet apex for given S and U. Using COMSOL simulations (Fig. 3 G and H), we determined E = 1.22 U/S at the sessile droplet apex (SI Appendix, Fig. S6A). Given the ice needles' stable cylindrical shape (Fig. 3F and SI Appendix, Fig. S5D), the surface area A could be calculated as  $A = 9\pi H^2/32$  and the electrostatic force acting on the ice needle becomes

$$F_e = 0.4\pi\varepsilon_0 kH^2 U^2 IS^2.$$
 [1]

As the needle elongated,  $F_{\rm e}$  exhibited exponential growth (Fig. 31). The critical crack force  $F_{\rm c}$  required for crack initiation follows the Griffith criterion (38-40):

В

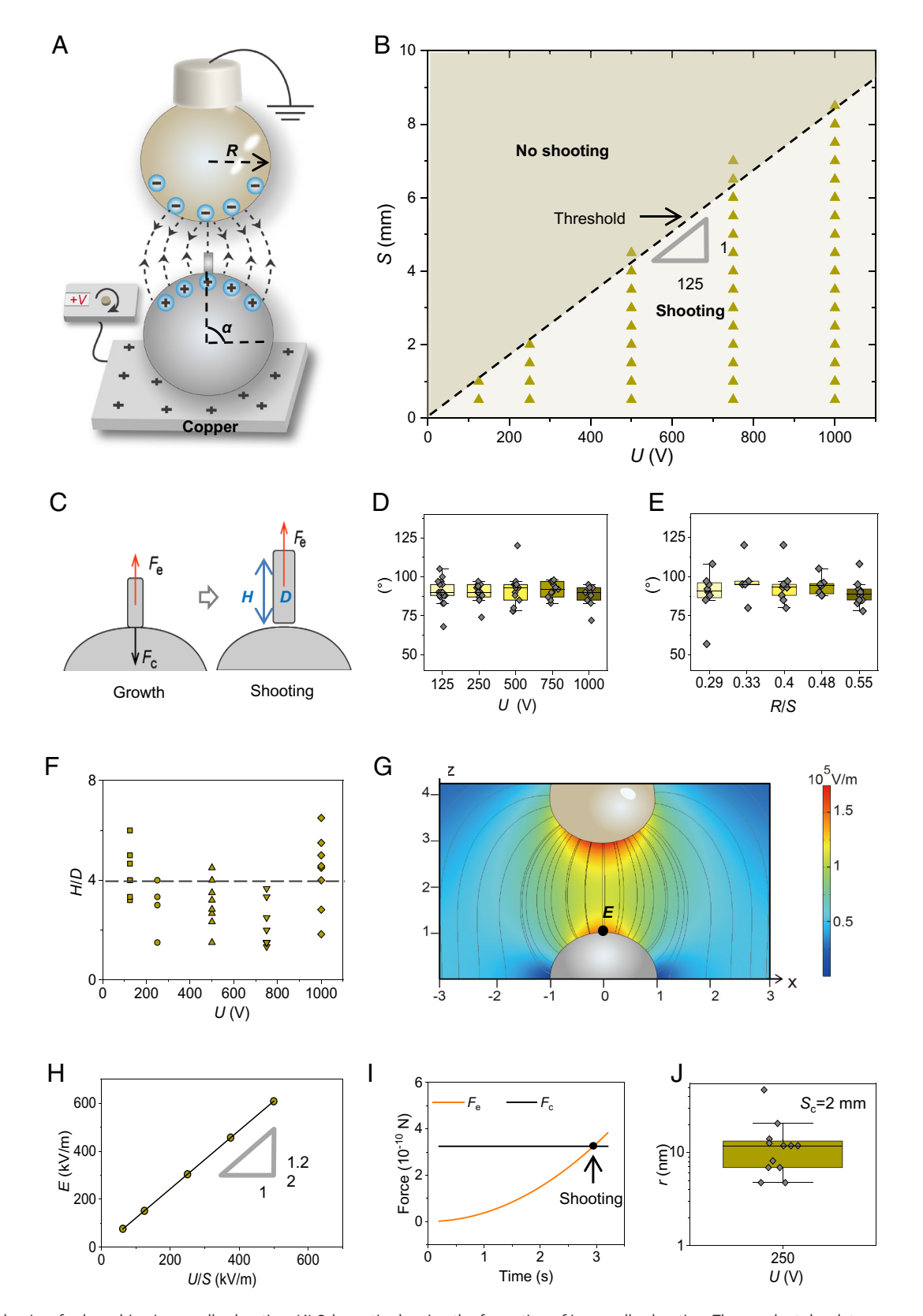
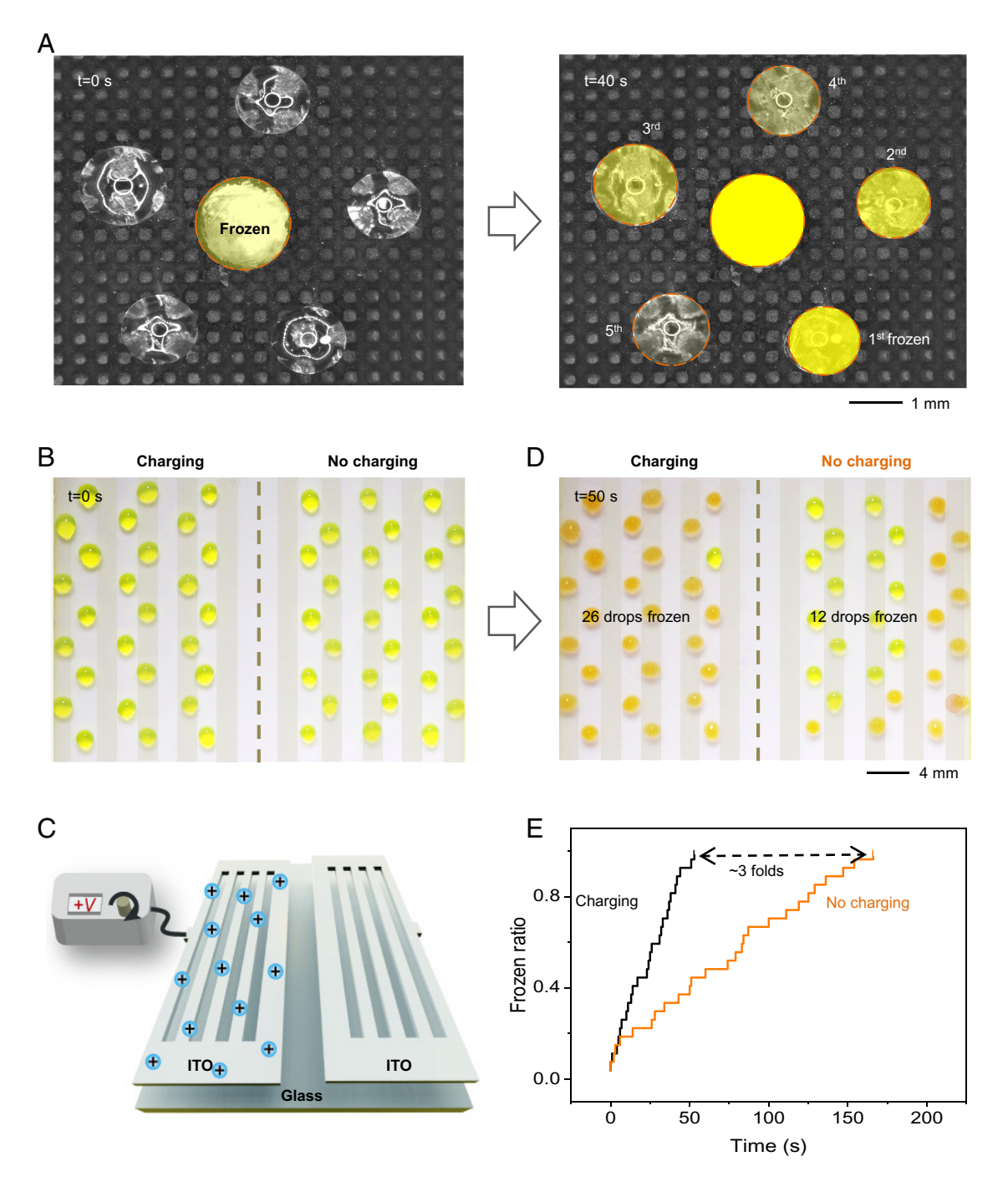


Fig. 3. Mechanism for launching ice needle shooting. (A) Schematic showing the formation of ice needle shooting. The pendant droplet was grounded, while the other droplet sat on a substrate connected to a positive voltage, which naturally formed an uneven electric field distribution between two droplets. (B) Phase diagram depicting the dependence of the ice needle shooting on droplet spacing S and voltage U. The filled and opened symbols denote the shooting and nonshooting regimes, respectively. (C) Schematic of forces exerted on the growing ice needle. (D) The ice needle shooting location under different voltage supplies and (E) the ratio of pendant droplet radius R to droplet spacing S. (F) The ratio of length H to radius D of the ice needle upon shooting. (G) Simulation results of the electric field distribution at U = 250 V. (H) The numerically obtained electric field intensity E at the peak of the frozen droplet is proportional to U/S. (/) Variation in the calculated forces exerted on ice needle growth, and (/) the calculated nucleating crack radius of the ice needles upon shooting under a critical shooting condition U = 250 V, S = 2 mm.



**Fig. 4.** Controllable and scalable IFR. (*A*) Optical image showing the rapid freezing of sparsely distributed droplets (3 μl) placed on a superhydrophobic and nonconductive FEP pillar array surface, with a small hollowed-out region in the center exposing the underlying hydrophilic and conductive aluminum substrate. A single droplet was deposited in this conductive region, while the remaining five droplets were placed in the nonconductive FEP surface. After the freezing of a single droplet in the conductive region, the other five droplets placed in the nonconductive FEP area were triggered to freeze almost simultaneously. (*B–D*) Optical images and schematic showing droplet arrays deposited on a glass substrate decorated with patterned comb-like indium tin oxide (ITO) electrodes. The *Left* part was connected to a voltage supply of 500 V, while the *Right* part remained uncharged. Nearly all droplets in the charged region got frozen within 50 s, turning orange, whereas fewer than 50% of the droplets in the uncharged region underwent freezing. (*E*) The charged part achieved a global surface freezing rate three times higher than its uncharged counterpart. Time zero corresponds to the moment when the first droplet began freezing. Ambient temperature: 10 to 15 °C; relative humidity: less than 40%; surface temperature: −5 °C.

$$F_{\rm c} = \sqrt{8\pi W_{ad} r^3 E_i / \left(1 - V_{i}^2\right)},$$
 [2]

where r is the nucleating crack radius and considered constant under a given U and S,  $w_{\rm ad}$  is the adhesion energy to create double ice–air interfaces (0.2 J/m<sup>2</sup>),  $E_{\rm i}$  is the Young's modulus (8.7 × 10<sup>9</sup> Pa), and  $v_{\rm i}$  is the Poisson's ratio of ice (0.31). By equating the electrostatic force and the critical crack force under shooting

conditions,  $F_{\rm e}=F_{\rm c}$ , we found that the threshold of ice needle shooting was governed by the interplay between U and the maximum shooting distance,  $S_{\rm max}=k~U$ , where  $k=1.95\times 10^{-12}r^{0.75}$ . Such a linear relationship between  $S_{\rm max}$  and U aligned closely with the experimental finding in Fig. 3B, with a slope of 1/125. The validity of our model was further supported by substituting 1/125 into the expression for k', yielding a nucleating crack radius of r=15 nm (Fig. 3J and SI Appendix), which was consistent with

previously reported values (38, 40) (r = 10 nm). After complete cracking, the in-air shooting dynamics of the ice needle was dominated by the electric force, similar to the behavior observed using dielectric substrates (details in SI Appendix, Figs. S7 and S8 and SI Appendix).

We further found that ice needle shooting behavior remains largely unaffected across a wide range of droplet sizes at fixed spacing and voltage. Key parameters such as needle length (SI Appendix, Fig. S9A) and velocity (SI Appendix, Fig. S9B) show minimal variation. However, when the droplet size approaches a planar water film, a decrease in shooting velocity occurs due to electric field redistribution (SI Appendix, Fig. S9C). This suggests that while the effect is robust, extreme droplet geometries may weaken field localization and slightly reduce shooting efficiency.

Controllability and Scalability of IFR. Finally, we showcased the controllability of the IFR phenomenon and its advantages for on-demand droplet freezing path, sequence, and scalable surface freezing regulation. Traditional freezing bridging typically follows a fixed path, propagating along the surface toward the nearest droplet in a sequential manner akin to a cascading domino effect. In contrast, our approach enabled customizable ice shooting paths (SI Appendix, Fig. S9 A-D and Movie S5) and adjustable droplet freezing sequence, which allowed the freezing of distant droplets prior to proximal ones (SI Appendix, Fig. S10 E-G and Movie S5), a capability unattainable with conventional freezing bridging. We further demonstrated that the freezing of a single droplet could trigger the nearly simultaneous freezing of multiple droplets dispersed across a surface with varying conductivity and wettability (Fig. 4A). The surface primarily consisted of a superhydrophobic and nonconductive FEP pillar array, with a central hollowed-out region exposing the underlying hydrophilic and conductive aluminum substrate connected to a power supply. After the droplet in the conductive region froze, five adjacent droplets in the nonconductive FEP area froze rapidly. This global surface freezing process completed within 40 seconds—one-third the time required for conventional freezing bridging (SI Appendix, Fig. S11 A–C and Movie S5).

To validate the scalability of the IFR phenomenon, we conducted freezing experiments using droplet arrays deposited on a glass substrate decorated with patterned comb-like indium tin oxide (ITO) electrodes. For comparison, two identical patterned indium tin oxide (ITO) electrodes were fabricated. The left electrode was connected to a voltage supply of 500 V, while the right electrode remained uncharged (Fig. 4 B and C). Each comb structure had a width of 2 mm and a spacing of 2 mm (SI Appendix, Fig. S10D). Both electrode parts were adorned with 27 dyed water droplets with a volume of 2 µl, initially appearing transparent and yellow. To inhibit interdroplet freezing bridging while maintaining surface charge gradient between ITO and glass strides, droplets were placed every two stripes in each row. We observed that nearly all droplets in the charged region got frozen within 50 s, turning orange. In contrast, less than 50% of droplets in the uncharged region became frozen during the same time (Fig. 4D). Remarkably, the charged section achieved a global surface freezing rate three times higher than its uncharged counterpart (Fig. 4*E* and Movie S6).

Given the ubiquitous presence of surface charges in nature and their ability to mobilize or levitate snow and ice particles, the spontaneous, charge-driven IFR phenomenon may play a critical role not only in atmospheric phenomena (41)—especially in thunderstorms, where ice, supercooled droplets, and electrostatic effects coexist (42, 43)—but also in practical applications. Importantly, the feasibility of this mechanism extends to real-world systems where strong electric fields and phase change coexist, such as high-voltage transmission lines exposed to humid, freezing conditions (44, 45), or cryopreservation systems where control over nucleation and growth is essential. While the underlying physical mechanism appears robust, translating it into scalable technologies will require careful engineering of surface charge distributions and environmental conditions. Nonetheless, our findings offer a physical basis for addressing long-standing challenges in icing, suggesting promising strategies for mitigation and control in both natural and industrial systems.

### **Materials and Methods**

Materials. Dimethyl sulfoxide (Solarbio, 99.5%), ethyl alcohol (Sigma Aldric, 99%), ethyl acetate (Sigma Aldric, 99.8%), isopropanol (Sigma Aldric, 99.7%), acetone (Sigma Aldric, 99.5%), acetic acid (Sigma Aldric, 99.7%), NaOH (Sigma Aldric, 0.01 M), NaCl (Sigma Aldric, 99.5%), petroleum ether (Sigma Aldric, 99.5%), hexyl hydride (Sigma Aldric, 99.5%), Agl (Sigma Aldric, 99%), fluorescent dye (MedChemExpress, 98.6%); PTFE plate, FEP plate, Resin plate, PVC plate, PS plate, PMMA plate, PVDF plate, PET plate, Glass plate, Nylon plate, TPU plate, copper plate, aluminum plate, titanium plate, and iron plate were commercial products purchased from vendors. All plates are the same size (length, 20 mm; width, 20 mm; thickness, 0.5 mm). The ITO glass with an ITO pattern thickness of 185 nm and sheet resistance of 6 was a commercially customized product (South China Xiangcheng Technology Company), and the ITO pattern (thickness, 185 nm) possessed a resistance of  $6\Omega$ .

**Fabrication of Substrates.** The PTFE substrate (20 mm  $\times$  4 mm  $\times$  0.5 mm), designed to show distinct charging patterns (Fig. 1A and SI Appendix, Fig. S3B), was first covered with clean copper tape and then cut with a 1 mm × 2 mm notch at its center. The resin substrate with millimeter-scale pillars (SI Appendix, Fig. S3D) was produced using a 3D printing method (BMF White-20 GR Resin, nanoArch S130 system, BMF Technology) based on photopolymerization. The FEP surface with micropillar array (Fig. 4A, and SI Appendix, Fig. S10 A and B) was fabricated following a set of controlled steps. The process started with an aluminum plate being processed to create an array of concave cavities, each with a diameter of 50  $\mu$ m and a depth of 500  $\mu$ m. The aluminum plate was then coated with 2 mm FEP particles, which were sprayed onto its surface. The coated aluminum plate underwent hot-pressing at 300 °C under 20 kPa pressure for 90 s, using the MFA F1540 system from Solvay company. The process ended with the demolding of the FEP micropillared structure from the aluminum plate. To make the FEP micropillared surface superhydrophobic, the surface was coated with a 50 nm layer of soot particles mixed in hexyl hydride (1 g/100 ml). Finally, a 1.5 mm diameter hole was drilled through the FEP substrate to expose the bottom aluminum layer.

Verification of IFR. To visualize the IFR phenomenon between two horizontally aligned droplets, the humidity in the transparent PMMA chamber (10 cm  $\times$  10 cm × 4 cm) was first reduced to below 40% using a humidity controller (Dataphysics HGC 20). The air temperature inside the chamber was finally stabilized between 10 and 15 °C after the cooling stage (Dataphysics TC 160) was turned on. Then, we attached a T-type thermocouple (accuracy ±0.1 °C, 5SC-TT, Omega) onto the chosen substrate with an insulating tape. The surface temperature was measured prior to the droplet freezing experiments. After setting the temperature of the cooling stage (approximately -12 °C), temperature data were recorded using a temperature data logger (RDXL6SD, Omega). During subsequent ice needle shooting experiments, the thermocouple was removed to avoid any impact on the electrostatic charge distribution on the surface. A 10  $\mu$ l droplet was then placed on the copper region adjacent to the groove until it completely froze. Following this, a water source was positioned above the frozen droplet to generate ice needles via desublimation. Once the water source was removed, another 10 µl water droplet was placed on the opposite side of the groove. The entire IFR process was captured using a CCD camera (Shenmiao ZWSP-4KHC) from a side view.

For the visualization of IFR phenomena occurring between two vertically aligned droplets (Fig. 1 C and D), the humidity in the PMMA chamber was controlled to remain below 40%, with the ambient temperature inside the chamber finally being maintained between 10 °C and 15 °C. The PTFE substrate

 $(20 \text{ mm} \times 4 \text{ mm} \times 0.5 \text{ mm})$  was cooled to  $-10 \,^{\circ}\text{C}$ , as measured by a thermocouple, before a 10  $\mu$ l water droplet was deposited onto it. Another 10  $\mu$ l droplet was suspended using a grounded microliter syringe to dissipate electrostatic charges. The temperature of the pendant droplet was monitored using a thermocouple (diameter: 80  $\mu m,$  KPS-T-0.08-1000-CZ) attached to the bottom of the needle near the pendant droplet's surface. The syringe's temperature was controlled using a custom-built refrigeration system with automatic feedback and control functions. Upon the onset of freezing in the sessile droplet, the refrigeration system was activated, cooling the pendant droplet to -2 to 0 °C within 1 min.

To study the temperature variation of the pendant droplet in the out-of-plane droplet configuration, the freezing and ice needle shooting events between two  $10\,\mu l$  droplets were simultaneously recorded. A CCD camera captured the process from the front, while an infrared camera (FLIR T1050sc) operating at 30 fps filmed from the opposite direction (SI Appendix, Fig. S2A).

Visualization of Ice Needle Shooting Trajectory. The ice growth and ice needle shooting dynamics were captured using a high-speed camera (nac MEMRECAM HX-6E) equipped with a macrolens (Canon, EF100 mm, f/2.8L IS USM). The frame rate was set as 5,000 fps (SI Appendix, Figs. S2B, S4C, S6B, and S7 A-F).

Verification of the Generality of Ice Needle Shooting. The verification of ice needle shooting feasibility enabled by different dielectric substrates was the same to the visualization of IFR phenomena occurring between two vertically aligned droplets. To verify the suppression of ice needle shooting on electrically neutralized substrates, the PTFE and nylon substrates were given a 5-s ionizing air blowing. To ensure the comparability of different materials in sponsoring ice needle shooting, all the substrates were cut to the same size, placed on the cryostage surface at -10 °C. To demonstrate the ice needle shooting could also trigger the freezing of a diverse range of water sources, the PTFE sheet (20 mm  $\times$  4 mm  $\times$  0.5 mm) was used as the substrate, and all liquid droplets were standardized to  $4 \mu l$ .

Visualization of Controllable and Scalable IFR. To visualize controllable ice needle shooting (SI Appendix, Fig. S9 A-D), a 4  $\mu$ l water droplet was initially deposited on a copper substrate at −10 °C on a cryostage. The shooting target, either arc-shaped or straight, was presoaked with water, grounded, and aligned vertically or obliquely—with the shooting location on the lower copper plate. The copper plate was then connected to a 500 V power supply, and the process was captured using a high-speed camera operating at 2,000 fps.

For the visualization of sequentially adjustable droplet freezing (SI Appendix, Fig. S9 E-G), side-view experiments were carried out using CCD imaging. A 4  $\mu$ l water droplet was initially deposited on a copper plate (-5 °C) connected to a 1 or 2 kV voltage supply. Subsequently, two additional 4  $\mu$ l water droplets were placed on a PTFE plate with a droplet spacing of approximately 2 to 3 mm. The copper and PTFE plates were then aligned in parallel on a cryostage with a spacing of about 5 mm.

To film the freezing of a pentagon droplet pattern, a 4  $\mu$ l water droplet mixed with AgI particles at a ratio of 0.005 g/mL was first deposited on the exposed aluminum area of a FEP substrate with micropillar array at -5 °C. Simultaneously, five 3  $\mu l$  water droplets were arranged around it to form a pentagon. The substrate was then cooled. As the 4  $\mu$ l droplet began to freeze, a 500 V voltage supply (Dongwen High Voltage Power Supply Co., Ltd, DW-P303-1ACH2) was connected to the aluminum layer beneath the FEP layer. Once all droplets exhibited recalescence, the voltage supply was turned off (Fig. 4A and SI Appendix, Fig. S10 A-C). The entire surface was recorded at 30 fps using a CCD camera. To achieve condensation frosting based on freezing bridging only, the entire process was repeated once without turning on the power supply (inset in SI Appendix, Fig. S9C).

To film the freezing of a 27-droplet pattern (Fig. 4B-D), 27 dyed 2  $\mu$ l droplets (0.1 mg/mL) were first deposited on each side of the ITO device. The device was then cooled to -5 °C. Once the first droplet began freezing, a 500 V voltage supply was applied to the left side only. The entire process was recorded at 60 fps.

Simulation of the Electrostatic Field. To study the electrostatic field distribution around the PTFE substrate, we used finite-element method simulations with COMSOL Multiphysics 5.6. The electrostatic field was modeled using Maxwell's equations, simplified as  $\nabla \cdot \mathbf{D} = \rho V$ , and  $\mathbf{E} = -\nabla V$ , where  $\nabla$  represents the vector differential operator, D is the electric displacement field,  $\rho v$  is the voltage-dependent electric charge density, E is the electric field, and V is the electric potential. We simulated two configurations: one with a droplet on a dielectric material and the other with a droplet on a conductive material, and the corresponding model and boundary condition setting for the simulation were presented in updated SI Appendix, Fig. S4, here Fig. R5. The geometry was simplified as follows: the PTFE or Cu substrate was modeled as a rectangle (10 mm in width, 0.1 mm in height), and the pendant water droplet was represented by a circle with a radius of 1 mm, and ice droplet was represented by a semicircle with a radius of 1 mm. The droplets were spaced 2 mm apart, and the entire system was enclosed in a square (35 mm side length) representing the air domain. To minimize errors from the finite-sized model, we added a layer of infinite element domain (1 mm thickness, 1000x scaling) at the air domain's edge. The boundaries of pendant droplet and the air domain boundaries were grounded, and the frozen droplet and substrate were assigned a -250 V electric potential, based on the equipotential property of a stable charged object. The geometry was discretized into fine triangular mesh elements, and the electrostatic potential and field distributions were calculated using a linear solver with a tolerance of 0.001.

Data, Materials, and Software Availability. All study data are included in the article and/or supporting information.

**ACKNOWLEDGMENTS.** We acknowledge the financial support from the Research Grants Council of Hong Kong (no. 15237824, SRFS2223-1S01, C1006-20 W), the Natural Science Foundation of China Project (52333015), and the Meituan Foundation through the Green Tech Award.

Author affiliations: <sup>a</sup>Department of Mechanical Engineering, The Hong Kong Polytechnic University, Hong Kong 999077, China; <sup>b</sup>Department of Mechanical Engineering, City University of Hong Kong, Hong Kong 999077, China; Department of Aerospace Propulsion, School of Astronautics, Beihang University, Beijing 100191, China; Institute of Fundamental and Frontier Sciences, University of Electronic Science and Technology of China, Chengdu 611731, China; "State Key Laboratory of Fine Chemicals, Frontiers Science Center for Smart Materials Oriented Chemical Engineering, School of Chemical Engineering, Dalian University of Technology, Dalian 116024, China; and <sup>f</sup>Department of Aeronautics and Astronautics, Kyushu University, Fukuoka 8190395, Japan

- M. J. Kreder, J. Alvarenga, P. Kim, J. Aizenberg, Design of anti-icing surfaces: Smooth, textured or slippery? Nat. Rev. Mater. 1, 15003 (2016).
- C. S. Heu, H. Jang, J. Jeon, K.-S. Lee, D. R. Kim, Recent progress on developing anti-frosting and anti-fouling functional surfaces for air source heat pumps. Energy Build. 223, 110139 (2020).
- A. Dhyani et al., Design and applications of surfaces that control the accretion of matter. Science 373, eaba5010 (2021).
- C. Zhu et al., Direct observation of 2-dimensional ices on different surfaces near room temperature without confinement. Proc. Natl. Acad. Sci. U.S.A. 116, 16723–16728 (2019).
- X. Huang et al., Tracking cubic ice at molecular resolution. Nature 617, 86-91 (2023).
- H. Lambley et al., Freezing-induced wetting transitions on superhydrophobic surfaces. Nat. Phys. 19, 649-655 (2023).
- H. Zhang et al., Freezing droplet ejection by spring-like elastic pillars. Nat. Chem. Eng. 1, 765-773
- X. Yan et al., Unraveling the role of vaporization momentum in self-jumping dynamics of freezing supercooled droplets at reduced pressures. Nat. Commun. 15, 1567 (2024).
- F. Chu et al., Interfacial ice sprouting during salty water droplet freezing. Nat. Commun. 15, 2249 (2024).

- 10. S. Yang et al., Photothermal superhydrophobic copper nanowire assemblies: Fabrication and deicing/defrosting applications. Int. J. Extreme Manuf. 5, 045501 (2023).
- S. Yang et al., Condensation frosting and passive anti-frosting. Cell Rep. Phys. Sci. 2, 100474 (2021).
- S. Nath, S. F. Ahmadi, J. B. Boreyko, A review of condensation frosting. Nanoscale Microscale Thermophys. Eng. 21, 81-101 (2016).
- S. Jung, M. K. Tiwari, D. Poulikakos, Frost halos from supercooled water droplets. Proc. Natl. Acad. Sci. U.S.A. 109, 16073-16078 (2012).
- Y. Yao et al., Frost-free zone on macrotextured surfaces. Proc. Natl. Acad. Sci. U.S.A. 117, 6323-6329 (2020).
- R. Wen, Y. Ying, X. Ma, R. Yang, Sustainable anti-frosting surface for efficient thermal transport. *Cell* Rep. Phys. Sci. 3, 100937 (2022).
- S. Nath, J. B. Boreyko, On localized vapor pressure gradients governing condensation and frost phenomena. Langmuir 32, 8350-8365 (2016).
- H. Baytekin et al., The mosaic of surface charge in contact electrification. Science 333, 308-312
- Y. I. Sobolev, W. Adamkiewicz, M. Siek, B. A. Grzybowski, Charge mosaics on contact-electrified dielectrics result from polarity-inverting discharges. Nat. Phys. 18, 1347-1355 (2022).

- 19. Y. Jin et al., Complete prevention of contact electrification by molecular engineering. Matter 4, 290-301 (2021).
- W. Xu et al., A droplet-based electricity generator with high instantaneous power density. Nature **578**, 392-396 (2020).
- W. Xu et al., Triboelectric wetting for continuous droplet transport. Sci. Adv. 8, eade 2085 (2022).
- X. Yan et al., Bubble energy generator. Sci. Adv. 8, eabo7698 (2022).
- Y. Jin et al., Electrostatic tweezer for droplet manipulation. Proc. Natl. Acad. Sci. U.S.A. 119, 23. e2105459119 (2022).
- $H.\,Wu, S.\,Wang, Z.\,Wang, Y.\,Zi, Achieving\,\,ultrahigh\,\,instantaneous\,power\,density\,of\,\,10\,\,MW/m(2)\,by$ leveraging the opposite-charge-enhanced transistor-like triboelectric nanogenerator (OCT-TENG). Nat. Commun. 12, 5470 (2021).
- Q. Sun et al., Surface charge printing for programmed droplet transport. Nat. Mater. 18, 936-941 25. (2019).
- X. Li et al., Spontaneous charging affects the motion of sliding drops. Nat. Phys. 18, 713-719 (2022). 26
- 27 N. Miljkovic, D. J. Preston, R. Enright, E. N. Wang, Electrostatic charging of jumping droplets. Nat. Commun. 4, 2517 (2013).
- A. J. Weinheimer, A. A. Few, The electric field alignment of ice particles in thunderstorms. J. Geophys. Res. 92, 14833-14844 (2012).
- P. J. Connolly et al., Aircraft observations of the influence of electric fields on the aggregation of ice crystals. Q. J. R. Meteorol. Soc. 131, 1695-1712 (2005).
- S. Schmidt, J. D. Dent, A theoretical prediction of the effects of electrostatic forces on saltating snow particles. Ann. Glaciol. 18, 234-238 (2017).
- S. Panat, K. K. Varanasi, Electrostatic dust removal using adsorbed moisture-assisted charge induction for sustainable operation of solar panels. *Sci. Adv.* **8**, eabm0078 (2022).
- L. L. Cui et al., The comparative studies of charge storage stabilities among three PP/porous PTFE/PP electret. J. Electrostat. 67, 412-416 (2009).

- 33. S. Chavan et al., Effect of latent heat released by freezing droplets during frost wave propagation. Langmuir 34, 6636-6644 (2018).
- S. Yang et al., Efficient anti-frosting on discrete nanoclusters via spatiotemporal control of condensation frosting dynamics. Chem. Eng. J. 465, 142991 (2023).
- F. Chu, Y. Lin, X. Yan, X. Wu, Quantitative relations between droplet jumping and anti-frosting effect on superhydrophobic surfaces. Energy Build. 225, 110315 (2020).
- J. Chen, Z. L. Wang, Reviving vibration energy harvesting and self-powered sensing by a triboelectric nanogenerator. *Joule* 1, 480–521 (2017).
- H. Zou et al., Quantifying the triboelectric series. Nat. Commun. 10, 1427 (2019).
- S. F. Ahmadi, S. Nath, C. M. Kingett, P. Yue, J. B. Boreyko, How soap bubbles freeze. Nat. Commun. **10**. 2531 (2019).
- 39. H. Gao, H. Yao, Shape insensitive optimal adhesion of nanoscale fibrillar structures. Proc. Natl. Acad. Sci. U.S.A. 101, 7851-7856 (2004).
- R. Mukherjee, S. F. Ahmadi, H. Zhang, R. Qiao, J. B. Boreyko, Electrostatic jumping of frost. ACS Nano **15**, 4669–4677 (2021).
- L. Ulrike, J. Feichter, Global indirect aerosol effects: A review. Atmos. Chem. Phys. 5, 715-737 (2005).
- C. Saunders, H. Bax-Norman, C. Emersic, E. Avila, N. Castellano, Laboratory studies of the effect of cloud conditions on graupel/crystal charge transfer in thunderstorm electrification. Q. J. R. Meteorol. Soc. 132, 2653-2673 (2006).
- B. J. Mason, The Bakerian Lecture, 1971. The physics of the thunderstorm. Proc. R. Soc. Lond. A 327, 433-466 (1972).
- J. T. Bartlett, A. P. van den Heuval, B. J. Mason, The growth of ice crystals in an electric field. Z. Angew. Math. Phys. ZAMP 14, 599-610 (1963).
- V. Schaefer, R. Cheng, The production of ice crystal fragments by sublimation and electrification. J. Rech. Atmos. 5, 5–10 (1971).